HAIRPIN STRUCTURES IN A TURBULENT BOUNDARY LAYER WITH STRONG ADVERSE PRESSURE GRADIENT

M. H. Shafiei Mayam and Yvan Maciel
Department of Mechanical Engineering,
Laval University
Quebec City, G1K 7P4, Canada
ymaciel@gmc.ulaval.ca

ABSTRACT

Coherent structures in the outer region of a turbulent boundary layer subjected to a strong adverse pressure gradient have been studied using particle image velocimetry (PIV). The experimental set-up is designed to achieve flow conditions corresponding to trailing-edge stall of an airfoil. Large sets of instantaneous velocity fields are acquired by PIV in streamwise-wall-normal planes at three different streamwise locations. Signatures of hairpin vortices are found in all the fields and hairpin packets occur in the majority of them. The essential features of the hairpins and hairpin packets are similar to those found in zero-pressure-gradient turbulent boundary layers. The hairpin vortices are however slightly more inclined with respect to the wall in the present flow, and the upward growth of the hairpin packets in the streamwise direction is more important. The characteristics of the spanwise vortices are also documented.

INTRODUCTION

Although our understanding of canonical turbulent wall flows (zero-pressure-gradient turbulent boundary layer, fully developed pipe and channel flows) is far from complete, our knowledge of the details of turbulence in these flows has improved steadily over the past decades. It is nowadays generally recognized that coherent structures play an important role in the production of turbulence and in the transport of mass and momentum. For this reason, a large part of the recent research efforts focus on better understanding the properties, dynamics and interactions of coherent structures.

In contrast, not much is known about the characteristics and behaviour of coherent structures in adverse-pressure-gradient turbulent boundary layers (APG TBL). The numerous studies that exist have usually focused on the statistical properties of APG TBL. Recent studies of APG TBL using direct numerical simulations have provided some insight into the turbulent structures found in these flows (Spalart and Coleman 1997, Na and Moin 1998, Skote and Henningson 2002). However, these studies pertained to separation bubbles at very low Reynolds numbers with fairly rapid distortion of the upstream boundary layer. Moreover, the focus was only on the near-wall structures.

In zero-pressure-gradient turbulent boundary layer (ZPG TBL), many recent experimental and computational studies support the existence of hairpin structures in the log and wake regions. Adopting the terminology of Adrian et al. (2000), hereafter referred to as AMT, the term hairpin is used here as a general term to represent cane, hairpin, horseshoe or arch-shaped vortices, or any deformed versions of them, that induce ejection beneath their spanwise arch segment. AMT investigated the form and characteristics of single and multiple hairpins in a streamwise-wall-normal plane of the outer region of ZPG TBL. They showed that the hairpins generally occur in groups coherently aligned in the streamwise direction. They further proposed a conceptual model to explain the formation of hairpin packets. More recent studies on the subject are reviewed by Natrajan et al. (2007).

Understanding the behaviour of turbulence in turbulent boundary layers subjected to a strong adverse pressure gradient is no doubt of great technological interest. The objective of the present study is to gain a better understanding of coherent structures in the outer region of APG TBL. The particular flow case studied here is a turbulent boundary layer under external flow conditions similar to those found on the suction side of airfoils in trailing-edge post-stall conditions. It is therefore a high-Reynolds-number nonequilibrium TBL that has suffered from an abrupt transition from very strong favourable pressure gradient (FPG) to very strong APG, leading to a non-reattaching large separation zone. The statistical properties of this flow, in the APG zone up to separation, have already been studied by Maciel et al. (2006). Details of the experimental set-up and methods can also be found in that paper. In the present experiment, the measurements were made at three streamwise positions covering the APG region between the suction peak and the detachment point.

EXPERIMENTAL SETUP

In the following, it is assumed that the mean flow is in the x-direction, y-direction is perpendicular to the floor where the studied boundary layer develops and z is the spanwise direction.

The setup (figure 1) was designed to reproduce external flow conditions of airfoils for which separation starts at the trailing edge and gradually moves upstream as the angle of attack is increased. The reference pressure distribution used for the design was that of the conventional NACA 2412 airfoil set at an angle of attack of 18^o and at $Re_c = 2.5 \times 10^6$. It is important to note however that the aim was not to reproduce exactly the pressure distribution of the NACA 2412 airfoil but rather to reproduce qualitatively its features.

A system of splitter plates was used to control the lateral wall boundary layers and corner eddies in order to reduce significantly their effects on the floor boundary layer, figure 1a. Extensive PIV measurements and oil film visualisations were made to validate the flow. A description of these measurements and of the resulting analysis can be found in Maciel et al. (2006). It was found that the boundary layer at midspan and up to detachment essentially behaves as a two-dimensional boundary layer.

The PIV system consists of a 120 mJ ND: YAG laser (New Wave Research Solo, PIV 120) and two digital cam-

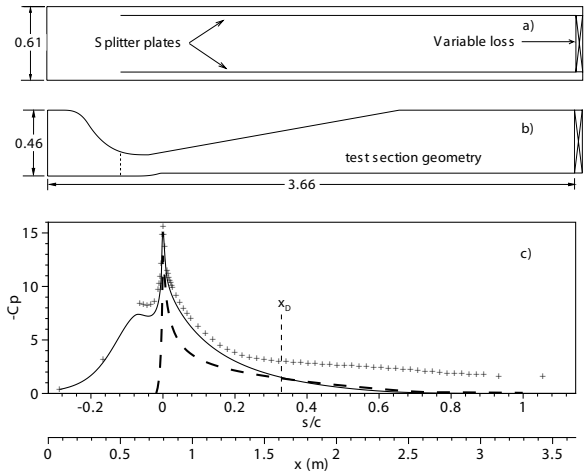

Figure 1: a,b Respectively top view and side view of the modified test section of the boundary-layer wind tunnel. Dimensions in m. c) Pressure coefficient distribution along the floor of the test section: ++ Measurement, −− NACA 2412 airfoil (2.5 m, 18^o), — Potential flow calculation

x(mm)	1156	1392	1600
Δx, Δy	0.19	0.39	0.66
Δx^+, Δy^+	6.6	7.6	
δ^+	765.9	836.7	
Re_θ	5329	8638	12095
β	4610	32200	
β_{ZS}	0.048	0.067	0.041
δ	21.03	42.78	73.72
δ^*	7.40	19.96	38.94
θ	4.12	7.50	10.34
U_{ZS}	7.78	8.95	9.63

Table 1: Vector spacings ($\Delta y = \Delta x$) and boundary layer parameters for the reference streamwise positions. Lengths in mm and velocities in ms^{-1}.

eras (HiSense Camera 1280×1024 pixels CCD array size). The PIV data processing was done with Dantec Dynamics FlowManager software and with Matlab. Image interrogation was done with adaptive cross-correlation (using FFT and iterations for offsetting the second interrogation window). The final interrogation area size was 16 pixel square with 50% overlap. Erroneous vectors were detected with the normalized median test technique of Westerweel and Scarano (2005). They were substituted but only if at least five valid vectors surround them. Substitution was done with a 2D least-square fit based only on the valid vectors surrounding the erroneous vector. A two-dimensional homogeneous Gaussian filter was finally used to smooth the instantaneous PIV velocity fields. Two sizes of the spatial filtering window were used depending on the analysis performed. The spatial filtering window was set at 0.025δ for the study of the hairpin vortices and packets, and 0.014δ for the study of the spanwise vortices.

A large streamwise dimension of the PIV measurement planes is necessary in order to study the hairpin packets characteristics. Thus the x-y dimensions of the PIV measurement planes were chosen to be about $3\delta \times 1.3\delta$ at each streamwise position (figure 2b). On the other hand, high spatial resolution is needed to resolve the velocity fluctuations and vortices. To increase the spatial resolution, measurements were made simultaneously with two overlapping large x-y planes (i.e. two cameras, see figure 2a) which when combined covered 3δ in the streamwise direction. Each camera therefore sees a region of about $1.6\delta \times 1.3\delta$. Matching of the instantaneous velocity vectors in the overlap zone was found to be always very good. Velocity and Reynolds stress profiles, as well as integral parameters of the boundary layer, were compared with those of the highly-resolved measurements of Maciel et al. (2006) and were also found to be in good agreement (figure 3).

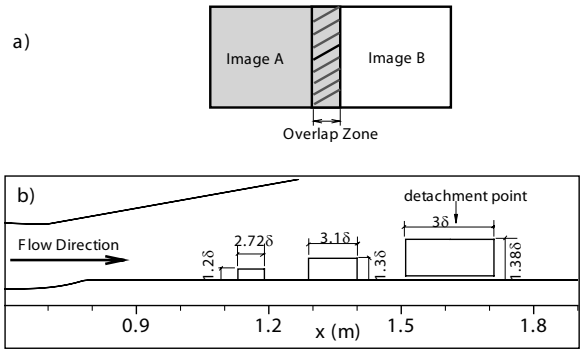

Figure 2: Measurement set-up: a) configuration of the two image planes, b) position of measurement planes.

Three streamwise locations, one in each PIV measurement plane, were selected to obtain detailed statistical information about the spanwise vortices. In order to ensure consistent results, these streamwise locations correspond to positions where the spatial resolution is identical in outer units (0.009δ). The vector grid spacing in physical units for these three stations is presented in Table 1, where it is also expressed in viscous wall units for the two most upstream stations. The last station is very close to the position where $C_f = 0$, which is $x = 1615$ mm. Table 1 also presents the most relevant boundary layer parameters, where U_{ZS} is the Zagarola-Smits outer velocity scale, $U_{ZS} = U_e\delta^*/\delta$; β_{ZS} is the pressure gradient parameter with ZS scaling, $\beta_{ZS} = -(\delta/U_{ZS})dU_e/dx$; β is the Rotta-Clauser pressure gradient parameter, $\beta = -(\Delta/u_\tau)dU_e/dx$ with $\Delta = \delta^* U_e/u_\tau$.

RESULTS AND DISCUSSION

Hairpin vortices and packets

The coherent structure identification technique of AMT was used to detect the presence of hairpins and hairpin packets. The first step is to perform Galilean decomposition of the instantaneous velocity vector fields using a constant advection velocity vector (U_c, V_c). The fields can then be visualized as if the viewpoint was from a reference frame moving at the advection velocity. If the advection velocity matches the velocity at the centre of a vortex, the vortex will appear as a pattern of nearly circular streamlines (figure 4). By viewing the fields with many different Galilean frames of reference, the spanwise vortex cores in various regions of the flow become apparent. In a ZPG TBL, the wall-normal advection velocity of the vortices is usually small and can be neglected. In the case of a TBL with a strong APG, the rapid growth of the boundary layer implies that wall-normal advection of the vortical structures is not necessarily small. For this reason, it was often needed to subtract also a wall-

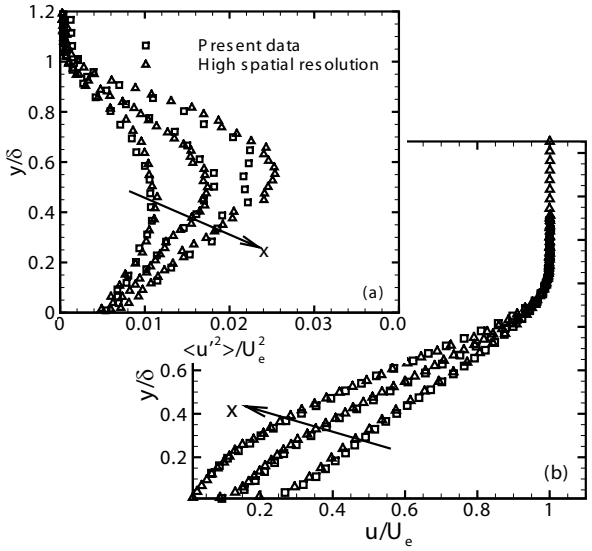

Figure 3: Profiles of a) streamwise Reynolds normal stress and b) streamwise mean velocity at the 3 streamwise positions of table 1. High-spatial resolution data from Maciel et al. (2006).

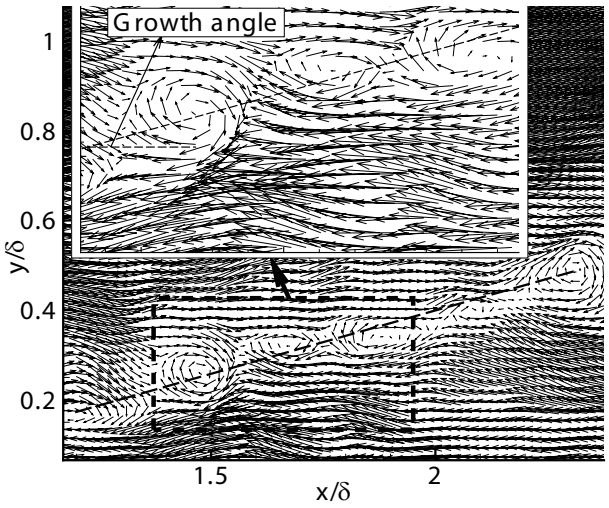

Figure 4: Instantaneous velocity field in region $x = 1.128 - 1.185$ m with Galilean decomposition $(u - 0.5U_e,\ v)$. One vector out of 4 for clarity.

normal advection velocity V_c, especially near the boundary layer edge, in order to clearly identify spanwise vortex cores.

Once vortices have been detected, one needs to discriminate the spanwise vortices that may be hairpin heads from the others. In a streamwise-wall-normal plane that cuts through the centre of a hairpin, the hairpin signature pattern, according to AMT, consists of a spanwise vortex core which is located above a region of second-quadrant Q2 vectors $(u-U_c < 0,\ v-V_c > 0)$, see figure 4. A fourth-quadrant Q4 region $(u-U_c > 0,\ v-V_c < 0)$ is habitually found to face the second-quadrant event from upstream, as can be seen in the inset of figure 4. The sharp frontier between the Q2 and Q4 events consists of a stagnation point that resembles a saddle point and an inclined shear layer.

More than 200 instantaneous velocity fields at each streamwise position were inspected via the hairpin identification technique just described. Like in the ZPG TBL experiments of AMT, hairpin vortex signatures are present in all the vector fields. They can be found throughout the outer layer for all streamwise locations. Again like in the ZPG TBL case, they generally appear in groups of hairpins, with individual hairpins within one group travelling at nearly the same streamwise velocity (hairpin packets). Hairpin packets are also found throughout the outer layer for all streamwise locations.

Often two and sometimes three hairpin packets are present in one vector field at different heights above the wall. When this is the case, long zones of relatively uniform streamwise momentum exist within the packets like in the study of AMT. These researchers suggest that the long region of uniformly retarded flow in each zone is the backflow induced by the several hairpins in the corresponding packet. They also suggest that the packet closer to the wall is actually nested inside the packet directly above. In the region close to the wall, $y/\delta < 0.2$, the individual hairpins and the packets tend to be smaller than further away from the wall. In ZPG TBLs, Tomkins and Adrian (2003) have found that these structures exist even in the buffer layer and that they grow linearly with distance from the wall in the buffer and log layers.

The angle at which the plane formed by the head and neck of the hairpin is inclined to the wall can be estimated with the angle of the locus of the Q2 region beneath the head. This angle cannot however be determined with accuracy from the hairpin signatures. The values given here are therefore only rough estimates. In the present flow, the locus angle is found to vary between 50^o and 80^o for all streamwise positions. These values are higher than those found by AMT (30^o and 60^o). The hairpins are therefore more inclined in the present flow. Like in the ZPG TBL, the locus angle tends to increase with distance from the wall.

AMT found that the hairpin packets grow upwards in the streamwise direction at a mean angle of about 12^o, with the angles ranging from 3^o to 35^o. These angles correspond to the angle between a line passing through the hairpin heads and the wall, figure 4. In the present flow, the growth angles are approximately between $15^o - 30^o$, with a mean value of 17^o. Note that the low angles obtained by AMT are usually found very near the wall, a zone where hairpins are not easily detected in our case. It is however clear from a comparison of the histograms of the growth angle in the two flows (not shown here) that the growth angles are higher in the present APG TBL.

The aforementioned differences between the ZPG TBL and the present strong APG flow can probably be explained by the fact that the mean strain rates are different in both flows. The velocity gradients $\partial U/\partial y$ (see figure 3) and $\partial V/\partial y$ are more important in the outer region of a strongly decelerated flow than in that of a ZPG TBL. Consequently, tilting and wall-normal stretching of the legs and necks of the hairpins should also be more important, leading to more inclined hairpins. Since the longer, most downstream hairpins in a hairpin packet are also normally the older ones, the increased titling and stretching also implies that the growth angle should be larger.

Spanwise vortices

In this section, the characteristics and population trends of the spanwise vortices are investigated in a manner similar to the study done by Wu and Christensen (2006) in ZPG TBLs and channel flows. Contrarily to what was done in the previous section, no distinction is made here between vortex

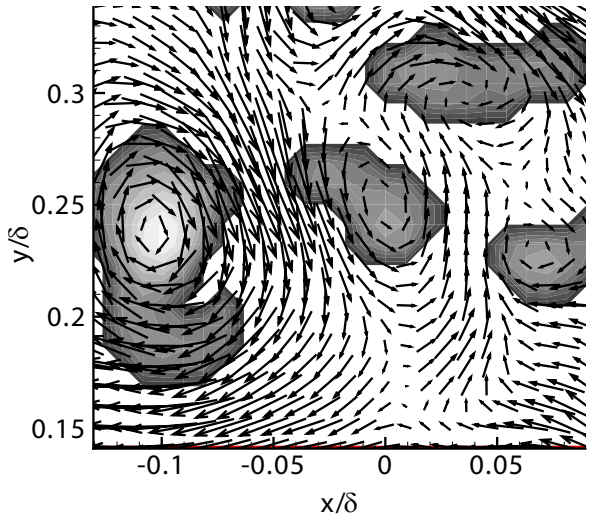

Figure 5: Example of vortex detection with the swirling rate. Galilean decomposition of the instantaneous velocity field. Contours of swirling rate.

cores that are hairpin heads and those that are not. Since it is desired to obtain detailed statistical information about the spanwise vortices, an automated procedure to detect these vortices is now used. The detection is done via the signed swirling rate, λ. The swirling rate is defined as the imaginary part of the eigenvalue of the local velocity gradient tensor (Zhou et al. 1999). Since the swirling rate does not indicate the sense of rotation, it is signed here according to the sign of the spanwise vorticity component. It has therefore a negative sign for prograde vortices (spanwise vortices with rotation in the same sense as the mean circulation).

To remove noise from the instantaneous swirling rate fields and to identify the boundaries of individual vortices, a threshold on λ has to be used. Wu and Christensen (2006) showed that in ZPG TBL and channel flows, the root-mean-square value of the swirling rate, λ_{rms}, is a representative scale of non-zero λ. They found that a threshold of $|\lambda/\lambda_{rms}| \geq 1.5$ defined well the boundaries of the vortex cores while minimizing experimental noise. In our case, the best threshold value was found to be 1.45. Because this criteria does not work well outside the boundary layer where vortices seldom occur, the threshold $|\lambda/\lambda_{max}| \geq 0.1$ is also used, where λ_{max} is the maximum of λ in the instantaneous field. Finally, only clusters with at least four contiguous points with non-zero λ were considered to form a vortex core. Figure 5 shows an example of vortex detection via swirling rate, where Galilean decomposition was applied to the vector field in order to reveal the vortices. Since a constant advection velocity was used, as opposed to a local one adjusted for each vortex, the vortex in the upper-right of the figure is not clearly revealed. When the local velocity at its position of maximum λ is used as the advection velocity, orbital streamlines become visible over this patch of swirl.

As mentioned in the Experimental setup section, three streamwise locations, one in each PIV measurement plane, were selected to obtain detailed statistical information about the spanwise vortices. In order to ensure consistent results, these streamwise locations correspond to positions where the vector grid spacing is identical in outer units (0.009δ). The vector grid spacing in physical and inner units, as well as the boundary layer parameters for these three stations are presented in Table 1.

Figure 6a presents the probability density functions

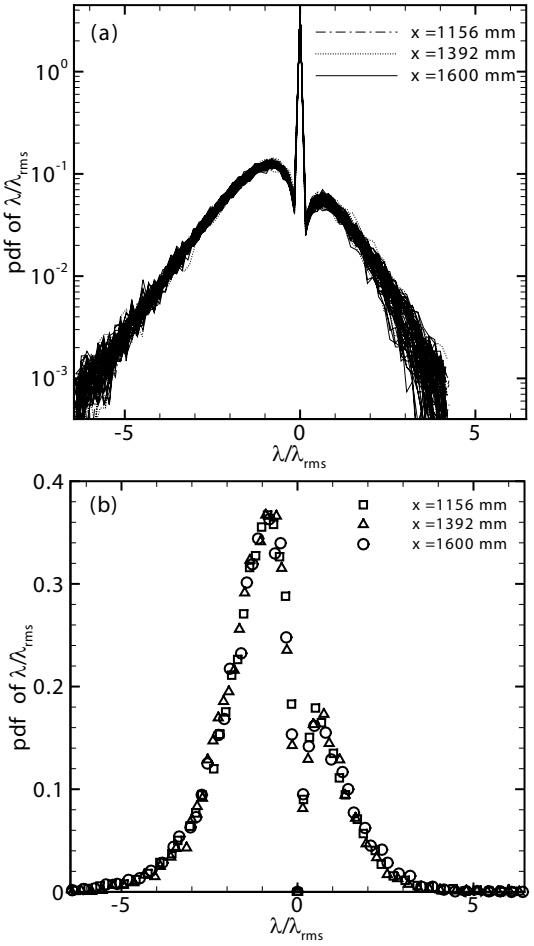

Figure 6: Probability density functions (pdfs) of λ/λ_{rms} at different streamwise positions, with no threshold applied : a) pdfs for $0.2 < y/\delta < 0.8$; b) pdfs obtained by excluding $\lambda = 0$ events from the samples, at $y/\delta = 0.5$.

(pdfs) of λ/λ_{rms}, when no threshold is applied, at the three streamwise stations and at several wall-normal locations in the region $0.2 < y/\delta < 0.8$. The probability of $\lambda = 0$ events is extremely high for all positions. Indeed, most of the surface of the flow fields does not contain swirling motions. The near collapse of the probability curves shows that λ/λ_{rms} is insensitive to x and y in the regions considered. Wu and Christensen (2006) obtained a similar insensitivity to y and Reynolds number in channel flows and ZPG TBLs. They concluded that λ_{rms} is a good scale for the magnitude of the swirling rate at a given x, y location. Our results confirm that it remains a good scale even when strong pressure gradients are present.

In order to analyze with more scrutiny the trends for prograde ($\lambda < 0$) and retrograde ($\lambda > 0$) vortices, figure 6b presents the pdfs of λ/λ_{rms} at $y/\delta = 0.5$ obtained by excluding $\lambda = 0$ events from the samples. As expected, prograde vortices are more frequent than retrograde vortices. The fact that the pdfs at the different streamwise locations collapse is an astonishing result. It means that although the vortices might change in size and swirl intensity, the probability of occurrence of vortices and the distribution of the normalized swirling rate, including the distribution between prograde and retrograde swirl, are unaffected by the varying strong adverse pressure gradient conditions. Moreover, this is the case all the way up to detachment since the last stream-

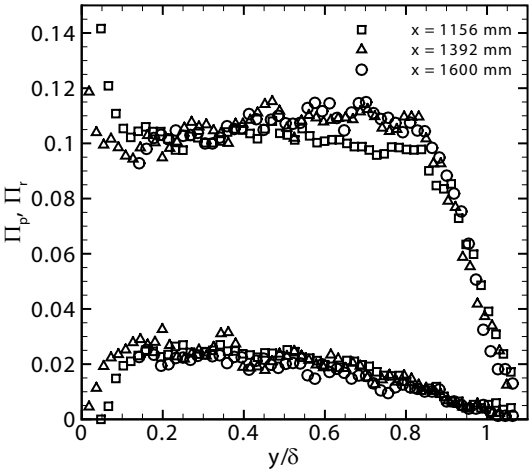

Figure 7: Probability of occurrence of prograde and retrograde vortices.

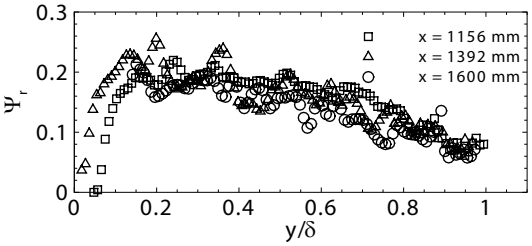

Figure 8: Fraction of retrograde vortices.

wise station is very close to the position of detachment of the boundary layer ($x = 1615$ mm). The population trends and distribution characteristics of the vortices are therefore persistent flow properties in such a flow.

Figure 7 illustrates the probability of occurrence of prograde and retrograde spanwise vortices, Π_p and Π_r, as a function of y/δ at the three different streamwise stations. These wall-normal trends reveal that the largest populations of prograde vortices occur near the wall (for the first two stations where measurements exist in that region) with a sharp decrease as we move away from the wall. The sharp decrease in Π_p stops around $y/\delta = 0.1$ for the first two stations. Further away from the wall, the profiles of Π_p are similar for the three stations, with an approximately constant value of $\Pi_p \approx 0.1$ in the region $0.1 < y/\delta < 0.8$ and a sharp drop close to the boundary layer edge. The degree of similarity revealed by these profiles is again astonishing for a TBL in fairly strong non-equilibrium conditions.

At this point, a qualitative comparison can be made with the profiles of vortex population densities obtained by Wu and Christensen (2006) in their ZPG TBL experiments. A quantitative comparison cannot be done because of the different parameters used in both studies: pointwise probability in our case, surface density for Wu and Christensen. The near-wall behaviour of Π_p is found to be qualitatively similar to that of the prograde vortex population densities obtained by Wu and Christensen. However in their case, the population densities continue to decrease monotonically for $y/\delta > 0.1$, but at a much slower rate than near the wall.

According to Wu and Christensen, these wall-normal trends can be explained by two possible scenarios. First, the average streamwise spacing between prograde vortices seems to increase as these vortices grow away from the wall and advect. In the second scenario, the monotonic decrease of population density with y would be due to the vortex merging mechanism which would predominantly take place in the outer region. We may also offer a complementary explanation that in canonical turbulent wall flows, a large portion of the prograde vortices are generated near the wall and that a fraction of them do not evolve away from it.

A clear difference therefore exists between the outer regions of this APG TBL and the ZPG TBL. In this APG TBL, the population of prograde vortices remains fairly constant in the region $0.1 < y/\delta < 0.8$ while it monotonically decreases in the ZPG TBL cases studied by Wu and Christensen. One possible explanation for this difference can lie in the fact that the prograde vortices are advected away from the wall faster in a strong APG TBL. As a result, the aforementioned scenario of vortex pairing may be less important in a strong APG TBL than in a ZPG TBL. As for streamwise dispersion of the vortices, it does not seem to vary significantly with y in the present flow.

In the near-wall region, the probability of occurrence of prograde vortices is greater for the first station than the second. As the fluid moves downstream, the generation of spanwise vortices near the wall might slow down since the dominant production mechanisms of turbulence are gradually shifting away from the wall. The near-wall differences in Π_p between the first and the second stations could also be due to the fact that an outer scaling with δ has been used. However, the near-wall trends observed in figure 7 remain even if inner scaling is used. In the ZPG cases of Wu and Christensen, the near-wall trends exhibit a strong Reynolds-number dependency when inner scaling is used.

Turning now our attention to the population trends of retrograde vortices, the profiles of Π_r (figure 7) are also found to be remarkably similar for the three streamwise stations. These populations trends are qualitatively very much alike those of the ZPG TBL. In both types of flows, the population of retrograde vortices grows away from the wall up to $y/\delta \approx 0.2$ and then gradually decreases.

The profiles of the fraction of retrograde vortices, Ψ_r, are presented in figure 8. As expected from the trends of Π_p and Π_r shown in figure 7, the profiles of Ψ_r are also remarkably similar for the three streamwise stations for $y/\delta > 0.2$. At $y/\delta = 0.2$, 20% of the spanwise vortices are retrograde and this proportion drops to 10% near the edge of the boundary layer. In the ZPG TBL experiments of Wu and Christensen, the proportion of retrograde vortices was fairly constant at 25-30% for $y/\delta > 0.2$. Retrograde vortices seem therefore to be less prevalent in a strong APG TBL.

Natrajan et al. (2007) presented evidence that a portion of retrograde vortices have a well-defined spatial relationship with neighbouring prograde vortices in canonical wall-bounded turbulent flows. Like Hambleton et al. (2006), they found that the preferred orientation is a prograde spanwise vortex positioned downstream and above the retrograde core. They conjectured this pattern to be on occasion the imprint of an omega-shaped hairpin structure. In the strong APG TBL studied here, the hairpin vortices are probably more stretched as explained before. Omega-shaped hairpin structures would therefore occur less frequently. By studying conditional averages of the local velocity field around detected retrograde vortices, we have found no evidence of a preferred orientation between prograde and retrograde vortices, contrarily to Natrajan et al. (2007).

The reduced presence of omega-shaped hairpin structures may partly explain why the proportion of retrograde spanwise vortices is less in a strong APG TBL. Alternatively,

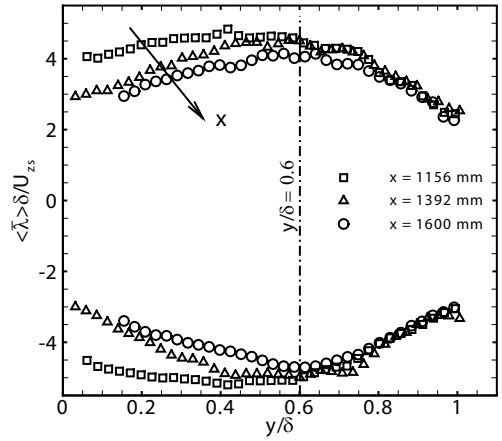

Figure 9: Ensemble average of $\bar{\lambda}$ normalized by U_{ZS}/δ.

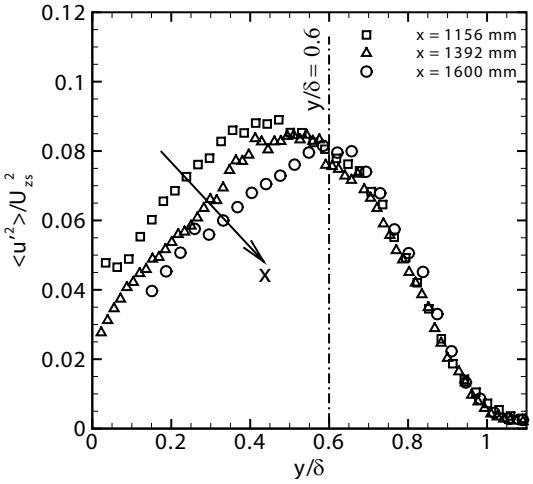

Figure 10: Streamwise Reynolds normal stress normalized using U_{ZS}.

as mentioned previously the merging of hairpin structures may be less frequent in a strong APG TBL. This would also translate into less retrograde spanwise vortices since vortex merging can generate isolated retrograde structures (Tomkins and Adrian, 2003).

In order to analyze the spatial distribution of the swirl intensity of the vortices, the average value of the swirling rate per vortex, $\bar{\lambda}$, was computed. Figure 9 presents the wall-normal profiles of the ensemble average of $\bar{\lambda}$ normalized by U_{ZS}/δ. The latter parameter can be considered to be the inverse of the outer time scale for the large-scale turbulent structures. Figure 9 shows that the prograde and retrograde spanwise vortices have approximately the same swirl intensity. It is also seen that the level of normalized swirl decreases in the streamwise direction in the region below $y/\delta = 0.6$ while it remains approximately constant above that region. Such a behaviour is consistent with that of the Reynolds stresses reported by Maciel et al. (2006). To illustrate this, figure 10 presents the profiles of $\overline{u'^2}$ normalized by U_{ZS} at the same streamwise positions. Streamwise evolutions of the profiles similar to those of the normalized swirl are observed. This suggests the strong link between the vortices and the Reynolds stresses, although the Reynolds stresses are second-order moments which are not solely the result of spanwise vortices.

CONCLUSION

Despite the presence of a very different pressure environment in this flow in comparison to the ZPG TBL, the gross features of the hairpin vortices and hairpin packets remain essentially the same, even as separation is approached. The hairpin vortices are however slightly more inclined with respect to the wall when the TBL is subjected to a strong APG, and the upward growth of the hairpin packets in the streamwise direction is more important. Contrarily to the situation in the ZPG TBL, the population of prograde vortices does not decrease with increasing wall-normal distance. The proportion of retrograde vortices with respect to prograde vortices is also less in a strong APG TBL. Tentative explanations for these various dissimilarities were given resting on the fact that the mean strain rates are more important in a strong APG flow.

Finally, the population trends of the spanwise vortices are found to be almost immutable in the outer region of the present flow. They are therefore persistent flow properties apparently unaffected by the pressure gradient.

ACKNOWLEDGEMENT

Financial support from NSERC and CFI of Canada is gratefully acknowledged by the authors. MHSM wishes to thank the Ministry of Science, Research and Technology of the Islamic Republic of Iran for its financial support via its scholarship program.

REFERENCES

Adrian, R. J., Meinhart, C. D., and Tomkins, C. D., 2000, "Vortex organization in the outer region of the turbulent boundary layer", *J. Fluid Mech.*, Vol. 422, pp. 1-54.

Hambleton, W. T., Hutchins, N., and Marusic, I., 2006, "Simultaneous orthogonal-plane particle image velocimetry measurements in a turbulent boundary layer", *J. Fluid Mech.*, Vol. 560, pp. 53-64.

Maciel, Y., Rossignol, K. S., and Lemay, J., 2006, "A study of a turbulent boundary layer in stalled-airfoil-type flow conditions", *Exp. Fluids*, Vol. 41, pp. 573-590.

Na, Y., and Moin, P., 1998, "Direct numerical simulation of a separated turbulent boundary layer", *J. Fluid Mech.*, Vol. 374, pp. 379-405.

Natrajan, V. K., Wu, Y., and Christensen, K. T., 2007, "Spatial signatures of retrograde spanwise vortices in wall turbulence", *J. Fluid Mech.*, Vol. 574, pp. 155-167.

Skote, M., and Henningson, D. S., 2002, "Direct numerical simulation of a separated turbulent boundary layer", *J. Fluid Mech.*, Vol. 471, pp. 107-136.

Tomkins, C. D., and Adrian, R.J., 2003, "Spanwise structure and scale growth in turbulent boundary layers", *J. Fluid Mech.*, Vol. 490, pp. 37-74.

Westerweel, J., and Scarano, F., 2006, "Universal outlier detection for PIV data", *Exp. Fluids*, Vol. 39, pp. 1096-1100.

Wu, Y., and Christensen, K. T., 2006, "Population trends of spanwise vortices in wall turbulence", *J. Fluid Mech.*, Vol. 568, pp. 55-76.

Zhou, J., Adrian, R. J., Balandar, S., and Kendall, T. M., 1999, "Mechanisms for generating coherent packets of hairpin vortices in channel flow", *J. Fluid Mech.*, Vol. 387, pp. 353-396.